Decoding functional cell–cell communication events by multi-view graph learning on spatial transcriptomics

Haochen Li[1], Tianxing Ma[2], Minsheng Hao[2], Lei Wei[2,*], and Xuegong Zhang[1,2,*]

[1] School of Medicine, Tsinghua University, Beijing 100084, China

[2] MOE Key Lab of Bioinformatics, Bioinformatics Division of BNRIST and Department of Automation, Tsinghua University, Beijing 100084, China

[*] To whom correspondence should be addressed: weilei92@tsinghua.edu.cn, zhangxg@tsinghua.edu.cn

Abstract

Cell–cell communication events (CEs) mediated by multiple ligand–receptor pairs construct a complex intercellular signaling network. Usually only a subset of CEs directly works for a specific downstream response in certain microenvironments. We call them functional communication events (FCEs). Spatial transcriptomic methods can profile the spatial distribution of gene expression levels of ligands, receptors, and their downstream genes. This provides a new possibility for revealing the holographic network of cell–cell communication. We developed HoloNet, a computational method for decoding FCEs using spatial transcriptomic data. We modeled CEs as a multi-view network, developed an attention-based graph learning model on the network to predict the target gene expression, and decoded the FCEs for specific downstream genes by interpreting the trained model. We applied HoloNet on two breast cancer Visium datasets to reveal the communication landscapes in breast cancer microenvironments. It detected ligand–receptor signals triggering the expression changes of invasion-related genes in stromal cells surrounding tumors. The experiments showed that HoloNet is a powerful tool on spatial transcriptomic data to help understand the shaping of cellular phenotypes through cell–cell communication in a microenvironment.

Introduction

Cell–cell communication is of vital importance to the organization and maintenance of multicellular organisms as well as the occurrence of diseases[1–3]. A cell–cell communication event (CE) occurs when sender cells release ligand molecules to the microenvironment and receiver cells sense the ligands by receptors. CEs form a complex intercellular signaling network that participates in the regulation of various genes. Abnormal CEs can trigger abnormal cellular phenotypes and may lead to the occurrence of many diseases[4,5].

A full picture of a CE should include the sender cell, the receiver cell, the ligand–receptor pair, and its downstream responses (**Fig. 1a**). It is worth noting that specific downstream responses are usually induced by only subsets of all possible CEs. We call such CE subsets functional communication events (FCEs) for their downstream targets. Decoding FCEs can help understand how specific microenvironments shape cellular phenotypes[6,7] and therefore is informative for studying possible disease interventions[8,9].

Current molecular profiling technologies provide bulk or single-cell gene expression profiles which include major ligand and receptor genes, cell-type-specific marker genes and possible downstream response genes. Recent spatial molecular profiling technologies such as spatial transcriptomic sequencing[10,11] and SeqFISH[12] can provide additional information about cell positions. Some data-driven methods have been developed to study CEs based on these technologies. For example, NicheNet[13] and MESSI[14] were built to characterize the relationship between ligand–receptor pairs and downstream responses, while NCEM[15] focused on the sender–receiver cell dependencies as well as the related phenotypes. A comprehensive understanding of FCEs should contain answers to the following questions: which cell types act as senders and receivers, where they are, and which ligand–receptor pairs they employ to induce what kind of downstream responses. However, a method for building such a holographic network of FCEs is still lacking.

In this work, we developed a computational method named HoloNet to reveal the holographic network of FCEs using spatial transcriptomic data. In HoloNet, we modeled CEs in spatial data as a multi-view network using the ligand and receptor expression profiles, developed a graph neural network model to predict the expressions of specific genes, and then interpreted the trained neural networks to decode FCEs. With spatial transcriptomic data and cell-type labels as the inputs, HoloNet provides a general workflow to characterize the communication landscapes in spatial data based on the multi-view CE network, and can identify cell types serving as major senders and ligand–receptor pairs serving as core mediators in FCEs for specific downstream genes. We applied HoloNet on two breast cancer datasets obtained with the 10x Visium technology[16]. The detected FCEs for specific gene expressions provided new insights into for how the microenvironment shapes cellular phenotypes in the corresponding tissues. HoloNet is available as a Python package at https://github.com/lhc17/HoloNet.

Results

Overview of HoloNet

HoloNet is a computational method for decoding FCEs using spatial transcriptome data. It requires spatial data, cell-type labels and paired ligand–receptor gene lists as inputs. The required spatial data should contain high-dimensional gene expression profiles and spatial positions of cells (**Fig. 1b**). Users can provide either continuous cell-type percentages derived from deconvolution methods such as Seurat[17] for spot-based datasets or categorical cell-type labels for datasets with single-cell resolution. We used the paired ligand–receptor gene lists from connectomeDB2020[18] as the default setting, but users can also provide gene lists from other databases.

HoloNet first constructs a multi-view CE network using the spatial data and paired ligand–receptor gene lists. As shown in **Fig. 1a**, in a CE, ligand molecules are released by the sender cell, diffuse over a distance within the tissue, and then bind to receptors expressed by the receiver cell. As cells communicate with others via multiple ligand–receptor pairs, CEs can be naturally modeled as a multi-view network. Each view in this network is a directed graph representing CEs mediated by one ligand–receptor pair with their own weighted edges. Each node represents a single cell or a spot in the measured tissue, and nodes across the multiple views are aligned. A directed edge in any view connects a sender cell to its corresponding receiver cell. An edge weight represents the strength of a CE mediated by the ligand–receptor pair between the sender and receiver cell. For each view, HoloNet calculates the weight of each edge by a function of three factors: the expression of the ligand in the sender cell, the expression of the receptor in the receiver cell, and the physical distance between the sender and receiver cell (**Fig. 1b**, **see "Methods" section**). HoloNet only retains edges with high confidence evaluated via a permutation test (**Supplementary Fig. 1a, see "Methods" section**).

HoloNet provides multiple approaches to analyze and visualize the multi-view CE network (**Fig. 1c**). For any ligand–receptor pair, HoloNet performs network-centrality analysis in the corresponding view to detect cells (or spots) with high communication activation as CE hotspots. HoloNet also constructs a cell-type-level CE network for each view which represents the general CE strengths from one cell type to another cell type. To explore the relationship between different ligand–receptor pairs, HoloNet quantifies similarities between different network views based on their local features and performs the hierarchical clustering method to cluster ligand–receptor pairs (**see "Methods" section**).

HoloNet can reveal a holographic network of FCEs based on the constructed multi-view CE network. We regard a CE as an FCE if the CE alters the expression of the gene of interest in the receiver cell. To decode FCEs, we decomposed the expression $\boldsymbol{E}$ of the target gene in all single cells or spots into its baseline expression $\boldsymbol{E}_0$ determined by its cell type and the expression change $\Delta\boldsymbol{E}$ caused by CEs triggered by multiple cell types and mediated by multiple ligand–receptor pairs (**Fig. 1a**). We employ multi-view graph neural networks (GNNs) to predict the expression profile of the target genes, and interpret the trained model to decode FCEs. **Fig. 1d** illustrates the procedure. We first obtained a matrix representing the cell type of each cell by one-hot encoding or the cell type percentages in each spot. Then, a GNN is constructed for each view by adopting the CE network of this view as the adjacency matrix and assigning each column of the cell-type matrix to the corresponding node in each graph as features. Embeddings of nodes of each view are integrated with the attention mechanism[19,20]. The integrated results are further fed into a fully connected layer to estimate $\Delta\boldsymbol{E}$. On the other hand, another fully connected layer is constructed to estimate $\boldsymbol{E}_0$ from the cell-type matrix.

The whole model is trained to minimize the difference between $\boldsymbol{E}$ and the sum of $\boldsymbol{E_0}$ and $\boldsymbol{\Delta E}$ (**Fig. 1d, see "Methods" section**).

After training, we interpret the attention weights of HoloNet to indicate which views in the multi-view network contribute more to the expression of a target gene. The ligand–receptor pairs corresponding to these views are regarded as the core mediators of FCEs regulating the target gene expression. All attention weights as well as their mean values across all trained models are visualized as the FCE mediator plot. We can further identify the major sender and receiver cell types in FCEs based on the graph convolutional layer to construct cell-type-level FCE connectivity networks (**Fig. 1e, Supplementary Fig. 1b, see "Methods" section**). To ensure the reliability of the findings, we repeated the training procedure for each target gene and integrated all the model-predicted gene expressions and model interpretation results.

In this article, we applied HoloNet on two human breast cancer spatial transcriptomic datasets. Both of them are based on 10x Visium technology. The dataset A is publicly available on the 10x Genomics website (**see "Methods" section for details**), and the dataset B is derived from a publication[16].

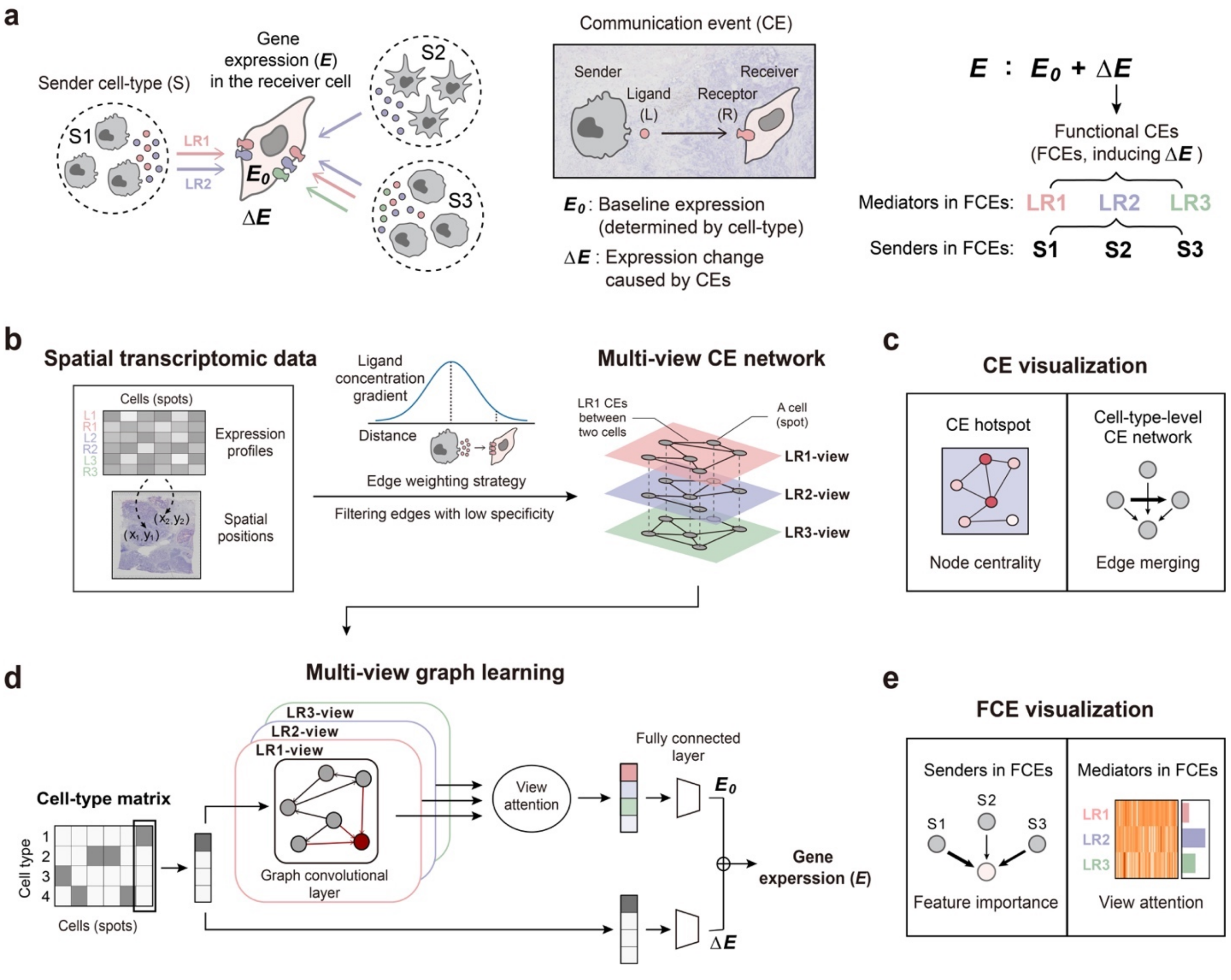

Fig. 1 The overall workflow of HoloNet.

a Definition of CEs and FCEs. **b** Constructing multi-view CE networks using spatial transcriptomic data. **c** As CE visualization, HoloNet provides CE hotspots and cell-type-level CE networks. **d** Predicting specific gene expressions via multi-view graph learning on the constructed multi-view CE network. **e** As FCE visualization, HoloNet identifies the core mediators and core senders of FCEs for specific genes.

Characterizing the cell–cell communication landscape in breast cancer Visium dataset A

We first showcased the functionalities of HoloNet on dataset A. The dataset is derived from an invasive ductal carcinoma breast tissue sample and profiled the expression of 24,923 genes in 3,798 spots. We calculated the cell-type percentage of each spot using the deconvolution method in Seurat[17] (**see "Methods" section**). The cell types include stromal cells, immunocytes, and tumor cells which are further divided into four cell types: basal-like-1 cells, basal-like-2 cells, luminal-AR cells and mesenchymal cells[21,22] (**Fig. 2a, b**).

We first constructed the multi-view CE network in the dataset by HoloNet. Here we took the ligand gene *COL1A1* and the corresponding receptor gene *DDR1* as an example (**Supplementary Fig. 2**). This ligand–receptor pair participates in diverse pathways related to tumor progression and metastases[23–25]. By visualizing the view corresponding to the COL1A1:DDR1 pair in the multi-view CE network, we found that there is active COL1A1:DDR1 communication in a protruding region between parenchyma (mainly including tumor cells) and stroma (mainly including stromal cells and immunocytes). In this region, the *COL1A1* signals from stromal cells and immunocytes are effectively received by tumor cells with highly expressed *DDR1*, causing some stromal cells and immunocytes to display prominent sender characteristics (**Fig. 2c, see "Methods" section**). The CE hotspots identified by degree centralities also revealed the protruding region with active COL1A1:DDR1 communication (**Fig. 2d**). We visualized CE hotspots by eigenvector centralities and found this approach could detect core CE hotspots more efficiently (**Supplementary Fig. 2d**). The cell-type-level CE network also indicated there are significant COL1A1:DDR1 signals sent from stromal cells and macrophages and received by basal-like-1 cells (**Fig. 2e**).

We quantified the similarities between network views according to their node eigenvector centrality vectors[26] and clustered ligand–receptor pairs into four groups (**Fig. 2f; Supplementary Fig. 3a, b; see "Methods" section**). We extracted Notch-related ligand–receptor pairs from the Hallmark gene sets of the molecular signatures database (MSigDB)[27], and found that these ligand–receptor pairs were assigned to two groups. The CE hotspots of the two groups of Notch-related ligand–receptor pairs covered different regions (**Supplementary Fig. 3c**). JAG2:NOTCH3 and MDK:NOTCH2 are the representatives of these two groups, respectively (**Supplementary Fig. 3d**). This result indicated that the Notch-related ligand–receptor pairs of two distinct groups could collaborate to control the Notch signaling in different regions.

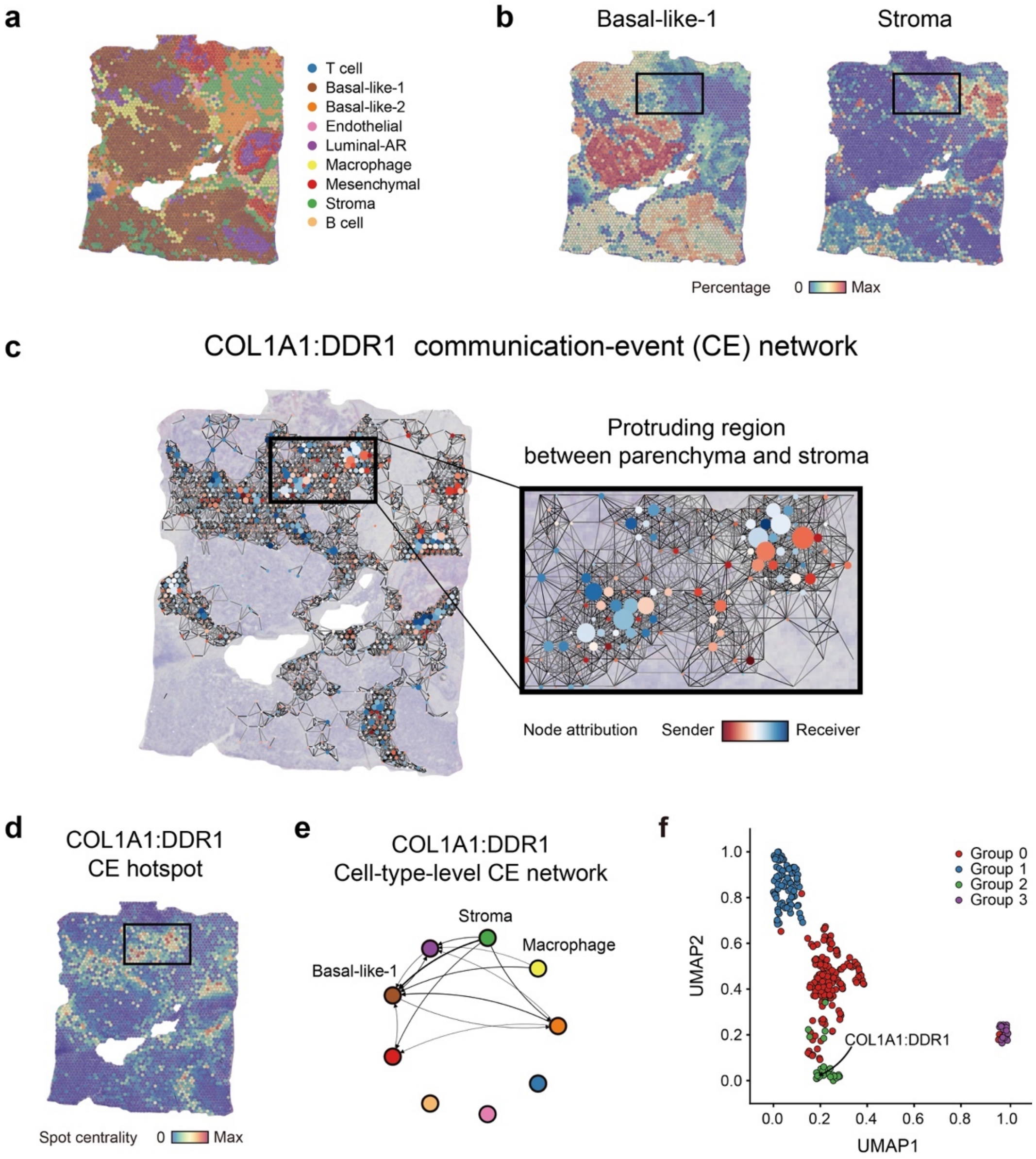

Fig. 2 Characterizing the cell–cell communication landscape of a breast cancer Visium dataset by HoloNet.

a The cell type with the highest percentage in each spot. Each dot printed on the slide represents a single invisible capture spot with a diameter of 55 μm. **b** The percentages of basal-like-1 and stromal cells in each spot. **c** The constructed single-view CE network based on the COL1A1:DDR1 pair. The size of a node indicates the degree centralities of the node in the network, and the color indicates the sender-receiver attribute of the node. The sender-receiver attribute is the result of subtracting the in-degree of a node from its out-degree. The redder the color of nodes, the more inclined the nodes are to act as a sender, and the bluer on the contrary. The thickness of an edge indicates the strength of CEs between cells linked by it. Nodes with too small size and edges with too low thickness are not displayed. Nodes are mapped to the spatial positions of their corresponding spots in the hematoxylin and eosin (H&E) stained histology image. **d** CE hotspot plot describes regions with active COL1A1:DDR1 signals. For (C), (D) and (E), the protruding region between parenchyma and stroma is highlighted. **e** Cell-type-level CE network plot describes the COL1A1:DDR1 communication landscape between cell types. The thickness of an edge reflects the summed weight of all edges in the CE network between the pair of cell types. **f** Low-dimensional representation of the eigenvector centrality vectors of each view plotted by UMAP. All ligand–receptors were hierarchically clustered into four groups based on the eigenvector centrality vectors.

The holographic network of FCEs related to *MMP11* expression pattern

Based on the multi-view CE network constructed from the breast cancer Visium dataset, we further applied HoloNet to decode FCEs. In breast cancer, cell–cell communication plays an important role in multiple biological processes such as tumor growth, invasion and migration, and leads various neoplastic and non-neoplastic cells in tumors to form complex heterogeneity[28,29]. However, there still lacks a systematic understanding of how the spatial expression patterns of functional genes are affected by cell–cell communication. For example, *MMP11* encodes matrix metallopeptidase 11 and is associated with worse overall survival through involving the degradation of the extracellular matrix[30,31]. Previous research found *MMP11* is expressed in stromal cells surrounding neoplastic cells[31,32], but it is unclear how neoplastic cells trigger the spatial expression patterns of *MMP11*.

We trained HoloNet to predict the expression of *MMP11*. As shown in **Fig. 3a**, the expression profile of *MMP11* predicted by HoloNet is quite similar to the pattern observed in the true spatial transcriptomic data. We noticed that *MMP11* is highly expressed in the lower-left part of the slide, where some stromal cells mix into tumor cells (**Fig. 3a**). To identify FCEs related to *MMP11* expression, we interpreted the multi-view graph neural network of the trained HoloNet by decomposing *MMP11* expression into baseline expression ($\boldsymbol{E_0}$) and expression change caused by CEs ($\boldsymbol{\Delta E}$). From **Fig. 3b**, we can see that the expressions of *MMP11* in stromal cells and macrophages are dominated by $\boldsymbol{E_0}$ while its expressions in the other cell types such as luminal-AR and basal-like-1 cells are largely determined by $\boldsymbol{\Delta E}$.

We found that the ligand–receptor pair POSTN:PTK7 always has the highest view attention weight in the multi-view network across multiple training replicates (**Fig. 3c**). This indicated that POSTN:PTK7 could be one of the core ligand–receptor pairs affecting *MMP11* expression. Besides, the CE hotspots of POSTN:PTK7 showed to highly coincide with the high-*MMP11* region (**Fig. 3d).** Based on the cell-type-level POSTN:PTK7 FCE network, we found that among all the edges linked to stroma, the one from basal-like-1 has the highest strengths, revealing that the basal-like-1 serves as the major senders of POSTN signals for triggering the change of *MMP11* expression level in stromal cells (**Fig. 3e**). The spatial plots of the POSTN:PTK7 FCE strengths for every cell types (**Supplementary Fig. 4**) show that the general FCEs from basal-like-1 cells form a spatial pattern similar to the actual expression pattern of *MMP11*. We also predicted the *MMP11* expression using several single-view CE networks and discovered that the CE with POSTN:PTK7 pair contributes more to determining the *MMP11* expression patterns than cell types or niches (**Fig. 3f**).

All the above results suggested that POSTN may regulate the expression of *MMP11* via PTK7, which is consistent with previous studies. POSTN has been found to be related to aggressive tumor behaviors via inducing angiogenesis or maintaining cancer stem cells in many cancer types including breast cancer[33–35]. It has been reported that *POSTN* is highly expressed in breast tumors, and higher expression of *POSTN* is associated with poorer clinical outcomes[35,36]. Meanwhile, PTK7 participates in the EGFR/Akt signaling pathway and upregulates *MMP11* expression in breast cancers[37]. In a study on head and neck squamous cell carcinoma, the POSTN:PTK7 axis has been found playing an important role in tumor progression and metastasis[38]. Some studies have employed the combination of *PTK7* and *POSTN* as an indicator of malignant progression[38,39]. We also verified that the expression level of *MMP11* has a positive correlation with the expression levels of *POSTN* and *PTK7* in breast cancer samples from TCGA data (**Supplementary Fig. 5a, b; see "Methods" section**).

We also identified some other ligand–receptor pairs that have been reported to be related to *MMP11* in previous studies. For example, we found that THBS1:ITGB1 and THBS1:PTPRJ serve as core ligand–receptor pairs affecting *MMP11* expression (**Fig. 3c, f**), and THBS1 that can alter *MMP11* expression in stromal cells is mainly contributed by basal-like-1 cells (**Supplementary Fig. 5c-f**). In previous studies, THBS1 has been shown to be able to stimulate *MMP11* expression in stromal cells and enhance oral squamous cell carcinoma invasion[40]. Researchers have reported that *THBS1*, *THBS2*, *POSTN*, *MMP11* can reflect the invasion phenotypes of breast tumors[41,42]. All those reported results supported the *MMP11*-related FCEs identified by HoloNet. In summary, HoloNet suggested a putative mechanism of how cell–cell communication affects *MMP11* expression: basal-like-1 cells serve as a major source of *MMP11*-level alteration in stromal cells via many ligand–receptor pairs such as POSTN:PTK7, THBS1:ITGB1 and THBS1:PTPRJ, which may be related to the alteration of stromal cells surrounding tumors into invasion-associated phenotypes (**Fig. 3g**).

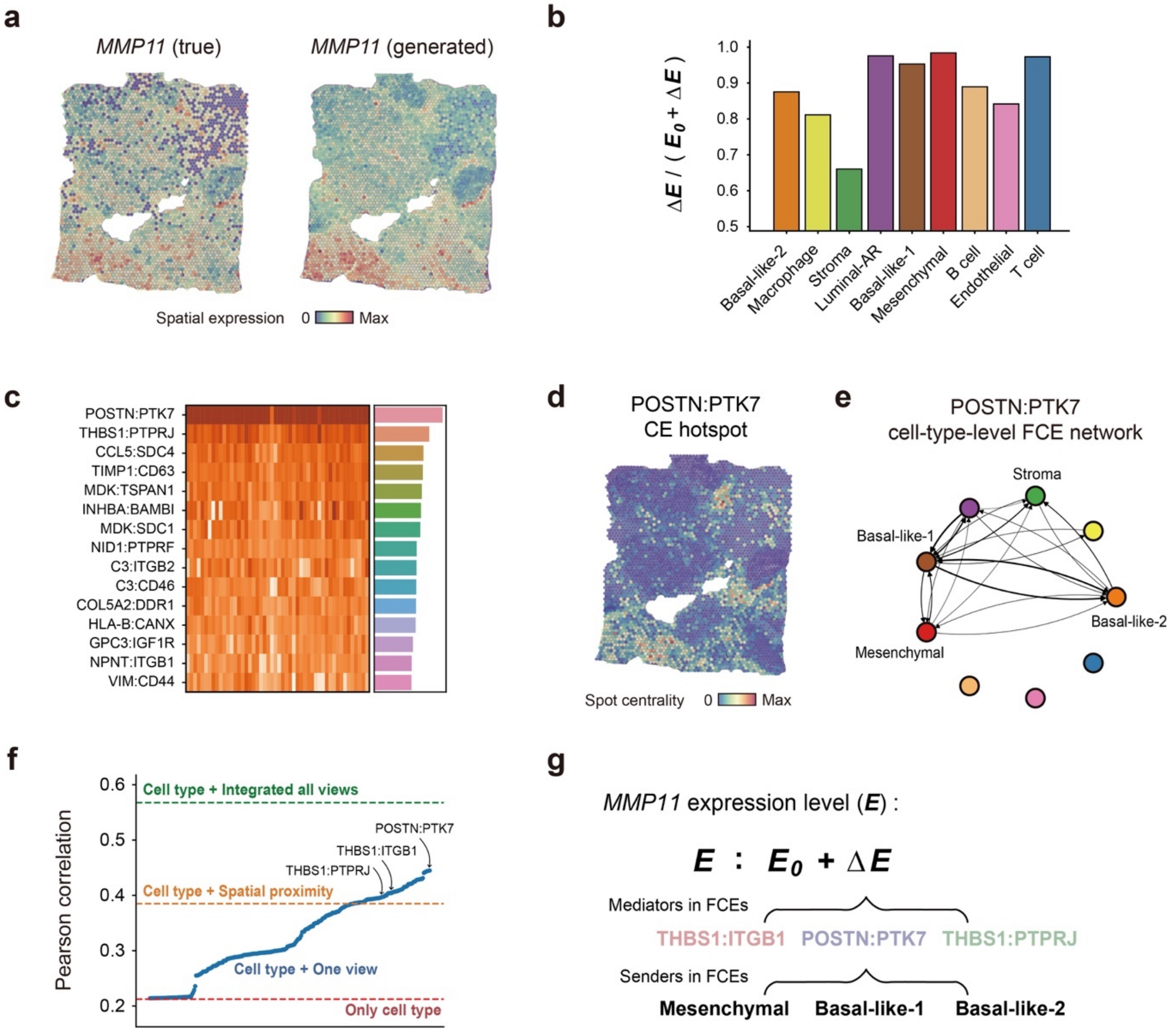

Fig. 3 Multi-view graph learning reveals the holographic network of how cell–cell communication affects gene expression patterns.

a The true (left) and HoloNet-predicted (right) expression profile of *MMP11*, preprocessed by log-normalization. **b** The ratio of the expression change caused by CEs ($\boldsymbol{\Delta E}$) to the sum of $\boldsymbol{\Delta E}$ and the baseline *MMP11* expression ($\boldsymbol{E_0}$) in each cell type. **c** Top 15 ligand–receptor pairs (286 pairs in total) with the highest view attention weights in the model predicting *MMP11* expression profile. The heatmap displays the attention weights of each view obtained from repeated the training procedure 50 times. The bar plot represents the mean values of the attention weights of each view. **d** The CE hotspot plot of POSTN:PTK7, showing the degree centrality of each spot in the POSTN:PTK7 CE network. **e** Cell-type-level POSTN:PTK7 FCE network for *MMP11*. The thickness of an edge represents the strength of ΔE contributed by POSTN:PTK7 between the two cell types connected by the edge. **f** Model performance in predicting *MMP11* expression using each single-view network (blue dots). The horizontal lines indicate the performances of the models only using cell-type labels (red), using cell-type labels and spatial proximity network (yellow), and using HoloNet (green). **g** The mechanism of multiple factors affecting *MMP11* expression revealed by HoloNet.

Identifying genes more affected by cell–cell communication

Besides *MMP11*, we applied HoloNet to other 566 highly variable genes to study how these genes are affected by cell–cell communication (**see "Methods" section**). Overall, by comparing the accuracy of gene expression prediction between models only using cell-type information (**see "Methods" section**) and those considering CEs, we found the prediction accuracy on almost all genes improved by considering CEs (**Fig. 4a**). Some genes, such as *MMP11*, showed higher improvements, indicating that they are more affected by CEs. The top 50 genes out of 567 genes with the highest improvements are enriched in gene ontology (GO) terms such as "cell–cell signaling" and "regulation of growth" (**Fig. 4b, see "Methods" section**). On the contrary, the bottom 50 genes with lower improvements are enriched in biological processes that are less sensitive to the external environment, such as "mRNA metabolic process" and "positive regulation of protein metabolic process" (**Supplementary Fig. 6a**).

Furthermore, similar to the case study on *MMP11*, for more than 90% of the used target genes, the ligand–receptor network brought better performances than the spatial proximity network, indicating ligand–receptor networks depicted the tissue microenvironments better than spatial proximity (**Supplementary Fig. 6b**). Meanwhile, HoloNet achieved a better performance than the Lasso regression model using both ligand–receptor communication and cell-type information (**Supplementary Fig. 6c**).

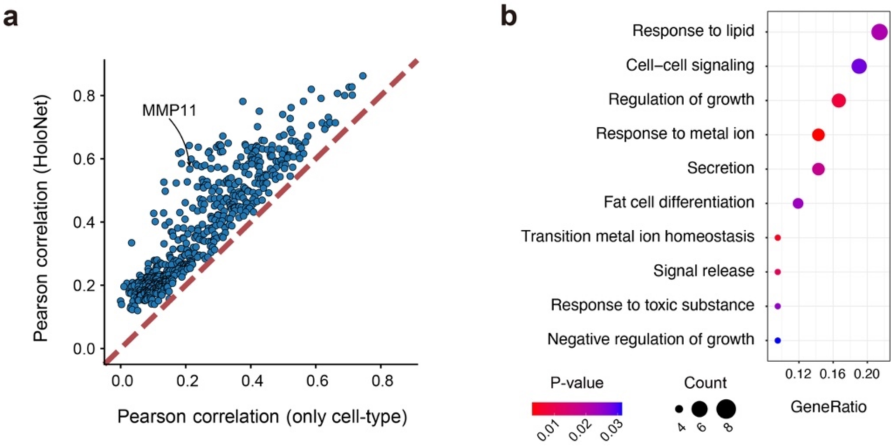

Fig. 4 HoloNet detects genes more affected by cell–cell communication.

a Performance comparison between HoloNet and models only using cell-type. The comparison is based on tasks for predicting the expression level of each gene. **b** Gene ontology (GO) enrichment for the top 50 genes with relatively higher performance improvements after considering CEs.

Application of HoloNet on the breast cancer Visium dataset B

We also applied HoloNet on the breast cancer Visium dataset B from a publication of Wu et al.[16]. We obtained the cell-type information of this dataset in the same way as the previous dataset (**Fig. 5a, see "Methods" section**), and trained HoloNet to predict the expression profiles of 285 highly variable genes. Similar to the results derived from the first dataset, we found that nearly all target genes are better predicted when considering the CEs (**Supplementary Fig. 7a**), and the top 50 genes out of 285 with the highest accuracy improvements are also enriched in communication-related GO terms such as "cellular response to stimulus" and "membrane organization" (**Fig. 5b**).

We chose *IGFBP7* as a case study in this dataset. This gene, *IGFBP7*, is a transporter of the insulin-like growth factor (IGFs)[43] and involves in angiogenesis, cell metabolism, and the progression of breast cancers[44,45]. We observed that *IGFBP7* is highly expressed in endothelial cells and stromal cells around endothelial cells in the spatial data (**Fig. 5c**). This indicates that stromal cells around blood vessels have high expression of *IGFBP7*, as endothelial cells cover the inner surface of blood vessels. To explore how cell–cell communication triggers the *IGFBP7* expression in stromal cells around blood vessels, we trained HoloNet to predict the expression of *IGFBP7* using HoloNet (**Fig. 5c**). After decomposing *IGFBP7* expression into baseline expression $\boldsymbol{E_0}$ and expression change $\boldsymbol{\Delta E}$ caused by CEs, we found the expressions of *IGFBP7* in endothelial and stromal cells are dominantly determined by $\boldsymbol{\Delta E}$ (**Fig. 5d**). We also found that some collagen-related ligand–receptor pairs such as TIMP1:CD63 and COL4A1:ITGB1 are always given the highest view attention weights (**Fig. 5e, f**), indicating they could be the core ligand–receptor pairs affecting *IGFBP7* expression. Based on the cell-type-level COL4A1:ITGB1 FCE network, we found that the macrophage, basal-like-1, and T cells serve as the major senders of COL4A1 signals that trigger the *IGFBP7* expression level change in stromal cells (**Fig. 5g**). The putative mechanism of how communication affects the *IGFBP7* expression in stromal cells around blood vessels is summarized in **Fig. 5h**. Previous research also reported that IGFBP7 is upregulated in the angiogenic vasculature[46], and collagens are also involved in angiogenesis[47,48]. Hooper et al. also found that IGFBP7 protein was localized to the vasculature or collagen type IV-rich compartments[46]. We also verified that the expression level of *IGFBP7* has a positive correlation with the expression levels of *COL4A1* and *ITGB1* in breast cancer samples from TCGA data (**Supplementary Fig. 7b, see "Methods" section**).

To confirm the results in dataset A, we predicted the expression profile of *MMP11* in dataset B (**Supplementary Fig. 7c**). Similar to the findings on dataset A, we also detected the layer corresponding to POSTN:PTK7 with the highest attention weight, and basal-like-1 cells serve as core senders in FCEs for *MMP11* (**Supplementary Fig. 7d-f**).

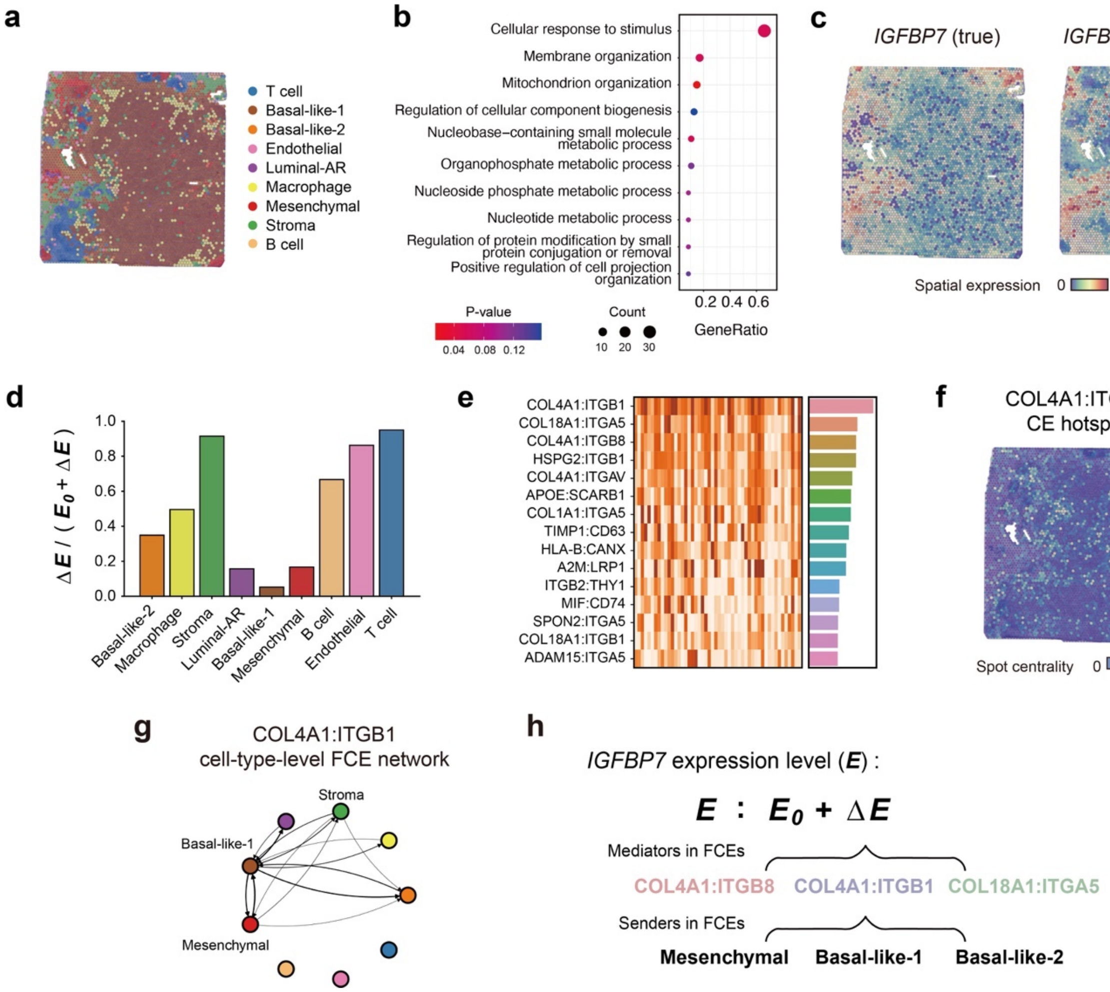

Fig. 5 HoloNet reveals the holographic network of how cell–cell communication affects *IGFBP7* expression pattern.

a The cell type with the highest percentage in each spot. **b** Gene ontology (GO) enrichment for the top 50 genes with relatively higher performance improvements after considering CEs, with all 285 genes as the background genes. **c** The true (left) and HoloNet-predicted (right) expression profiles of *IGFBP7*, preprocessed by log-normalization. **d** The ratio of the expression change caused by CEs ($\boldsymbol{\Delta E}$) to the sum of $\boldsymbol{\Delta E}$ and the baseline *IGFBP7* expression ($\boldsymbol{E_0}$) in each cell type. **e** Top 15 ligand–receptor pairs (138 pairs in total) with the highest view attention weights in the model predicting *IGFBP7* expression profile. The heatmap displays the attention weights of each view obtained from repeating the training procedure 50 times. The bar plot represents the mean values of the attention weights of each view. **f** The CE hotspot plot of COL4A1:ITGB1. **g** Cell-type-level COL4A1:ITGB1 FCE network for *IGFBP7*. **h** The mechanism of multiple factors affecting *IGFBP7* expression revealed by HoloNet.

Discussion

We developed a machine-learning method HoloNet to reveal the holographic network of cell–cell communication with spatial transcriptomic data. In HoloNet, we designed a multi-view network to model cell–cell communication events (CEs), built an attention-based graph learning model on the network to predict the target gene expression, and then interpreted the model to decode the functional CEs (FCEs). HoloNet provides the putative holographic network of how communication affects specific gene expression patterns, and answers a series of questions: which cell types act as senders and receivers, where they are, and which ligand–receptor pairs they employ to induce what kind of downstream responses. We applied HoloNet on two breast cancer Visium spatial transcriptomic datasets to verify its ability to offer new biological understandings. HoloNet revealed the cell–cell communication landscape in the breast tumor and detected ligand–receptor signals triggering the expression changes of some invasion-related genes in stromal cells surrounding tumors. We also identified a subtype of neoplastic cells serving as the primary senders of these signals.

Revealing a panorama of the communication, cooperation, and mutual influence among various cells in tissues is very important for understanding the operation of multicellular organisms and the development of diseases. We adopted the concept of CEs and FCEs as the core elements of the panorama. CEs describe the cell–cell communication with ligand–receptor pairs between any two single cells. FCEs are a subset of CEs, the CEs that affect specific downstream gene expression changes. The introduction of CEs and FCEs allows us to better characterize the whole process of intercellular communication from the sender cell to the receiver cell via the ligand–receptor pairs leading to specific downstream responses. Through the CE-centric approach, HoloNet can draw holographic cell–cell communication networks which could help to find specific cells and ligand–receptor pairs that affect the alteration of gene expression and phenotypes.

We have developed HoloNet as a user-friendly computational tool. It is developed as a Python package that can be easily installed and customized to facilitate the systematic exploration of CEs and FCEs in user-provided datasets. Users can follow our workflow: constructing the CE network among single cells, visualizing the communication landscape based on the network, predicting the expression patterns of genes of interest, identifying the major ligand–receptor pairs and sender cell-types in FCEs, and detecting the genes more affected by cell–cell communication. The main results in the article can be generated by our public python package.

HoloNet can help users solve many biological problems by revealing a holographic network of FCEs that affect the expression of genes of interest. For example, similar to the analysis presented in this article, users can use HoloNet to analyze how the expression profiles of cells are affected by other cell types in the microenvironment. Provided with pre- and post-treatment spatial transcriptomic data, users can also analyze how the treatment affects the full landscape of cell–cell communication within the tissue, understand unexpected treatment outcomes, and develop new disease interventions. With the widespread use of spatial transcriptomic techniques, HoloNet can be employed in an increasing number of biological scenarios to understand the holographic network of cell–cell communication in tissues and to analyze how cellular phenotypes are affected by FCEs.

In the future, we can incorporate prior knowledge embedding into the model, such as the intracellular signaling networks or known biological functions of some ligands, to better reveal how FCEs affect downstream gene expressions. In addition, with the development of spatial sequencing technologies, more subdivided cell types or positions on pseudotime trajectories can be used here to implement multi-scale models of FCEs and gain deeper biological understandings.

The core structure of HoloNet makes it possible to analyze various kinds of spatial transcriptomic data. For example, both single-cell-based spatial transcriptomic technologies such as SeqFISH and spot-based technologies such as 10x Visium can be easily used as the input of HoloNet. However, the current version of HoloNet acquires an adequate amount of cells or spots to train the GNN model, while the number of cells detected by SeqFISH[12] is too small to be well analyzed in HoloNet. Meanwhile, the number of genes profiled by MERFISH[49] is too small, so that HoloNet cannot construct CE networks using ligand and receptor gene expressions. We will continue to update HoloNet along with the development of spatial transcriptome technologies.

Methods

Datasets and data pre-processing

We applied HoloNet on two breast cancer 10x Visium datasets. The dataset A is from the 10x Genomics website (https://www.10xgenomics.com/resources/datasets, Visium Demonstration, Human Breast Cancer, Block A Section 1) and profiled the expression of 24,923 genes in 3,798 spots on a fresh frozen invasive ductal carcinoma breast tissue sample. The dataset B is obtained from the publication of Wu et al.[16]. They performed spatial transcriptomics on six samples, and we selected the 1160920F sample considering the cell-type richness and the number of spots. The dataset includes the expression profiles of 28,402 genes in 4,895 spots.
We excluded spots with less than 500 UMIs and genes expressed in less than 3 spots for both datasets and then normalized the expression matrix with the *LogNormalize* method in Seurat[17]. We annotated the cell types by label transfer (the *TransferData* function in Seurat) using a well-annotated single-cell breast cancer dataset (accession code is GSE118390)[21] as reference. The reference dataset contains four cell-types of malignant components (basal-like-1, basal-like-2, luminal-AR, and mesenchymal) and five cell-types of stromal and immune components (macrophage, B cell, T cell, stromal, and endothelial cell).

Multi-view CE network

Inspired by the concept of multi-view social networks[26,50,51], we used a node-aligned directed weighted multi-view network to represent CEs in spatial transcriptomics. Formally, a multi-view CE network G with a set V of views is defined on the aligned node set U. The node set U represents single cells (or spots) in the measured tissue. Each view $v \in V$ is a directed graph $G^{(v)} = (U, E^{(v)})$, in which $E^{(v)}$ consists of edges between nodes, and each edge $e_{i,j}^{(v)} \in E^{(v)}$ has a weight $\omega_{i,j}^{(v)}$ for $i, j \in U$. The edge weight $\omega_{i,j}^{(v)}$ is calculated by a designed edge weighting strategy, representing the strength of CEs from cell i to cell j mediated by a specific ligand–receptor pair corresponding to the view v. The multi-view CE network can be represented by a 3-dimension CE tensor (cell by cell by ligand–receptor pair) as a set of adjacency matrices $A^{(v)}$. The edge weight $\omega_{i,j}^{(v)}$ is the (i, j, v) element in the CE tensor. To optimize the computational efficiency, we used Pytorch[52] to implement the multi-view network in the following steps.

Edge weighting strategy

To calculate the edge weight $\omega_{i,j}^{(v)}$, we designed a new edge weighting strategy according to the law of molecular diffusion[53] and the law of mass action in chemistry. According to Fick's second law, considering a one-dimensional diffusion, the ligand concentration at x position and in time t is:

$$c(x,t) = \frac{N}{\sqrt{4\pi Dt}} e^{-\frac{x^2}{4Dt}}$$

where N is the number of "source" atoms per unit area initially placed at $x = 0$, and D is the coefficient of diffusion. This inspired us to model cell–cell communication in the spatial transcriptomic data using Gaussian functions. In spatial data, considering the ligand molecules (encoded by gene L_v) released by cell i (sender cell), the concentration of these ligand molecules at the position of cell j (receiver cell) is determined by the ligand expression in cell i and the distance parameter of cell i and j:

$$C_{i,j}^{L_v} \propto e_i^{L_v} \cdot \exp\left[-\left(\frac{dist_{i,j}}{w_{L_v}}\right)^2\right]$$

where cell i and cell j can be any cells in the spatial data, $e_i^{L_v}$ is the expression level of the ligand gene (L_v) in the sender cell i, $dist_{i,j}$ is the Euclidean distance between the spatial coordinates of the sender cell i and the receiver cell j, and w_{L_v} describes the diffusion ability of the ligand encoded by L_v which controls the covering region of ligands from one sender cell.

Here we set the proportionality coefficient as 1. Thus, for sender cell i, receiver cell j, and ligand–receptor pair v, the edge weight ($\omega_{i,j}^{(v)}$) is calculated as:

$$\omega_{i,j}^{(v)} = C_{i,j}^{L_v} \cdot e_j^{R_v} = e_i^{L_v} \cdot e_j^{R_v} \cdot \exp\,[-\left(\frac{dist_{i,j}}{w_{L_v}}\right)^2]$$

where $e_j^{R_v}$ is the expression level of the receptor gene (R_v) in the receiver cell j.

We also built up a relationship between our edge weighting strategy and the traditional strategy which only considers the cell–cell communication between neighboring cells within a fixed region. We selected w_{L_k} to make the amount of ligand molecules diffusing throughout the whole tissue equivalent to covering a region with a diameter (d) at a fixed concentration ($d = 255$μm as the default setting in Visium datasets, where the sender spot diameter is 55μm and ligands diffuse 100μm)[14,15]. Specifically, we let

$$\int_{-\infty}^{+\infty} (C_{i,j}^{L_v} / e_i^{L_v})\, d(dist_{i,j}) = d$$

Considering

$$\int_{-\infty}^{+\infty} \exp\,[-\left(\frac{dist_{i,j}}{w_{L_v}}\right)^2]\, d(dist_{i,j}) = \sqrt{\pi} \cdot w_{L_v}$$

we can get

$$w_{L_v} = d/\sqrt{\pi}$$

The specific value of w_{L_v} can be selected visibly by the *select_w* function in HoloNet (**Supplementary Fig. 1a**).

We obtained the information on ligands and receptors from connectomeDB2020[18]. The database categorizes ligands into plasma-membrane-binding and secreted ligands. We calculated the w_{L_v} of plasma-membrane-binding ligands by the aforementioned method, and set the w_{L_v} of secreted ligands twice as large as w_{L_v} of plasma-membrane-binding ligands by default. We filtered out ligand–receptor pairs in which either the ligand or the receptor expressed in less than 30% of the cells.

Filtering out edges with low specificities within a multi-view CE network

Both the effects of non-specifically widely expressed ligands (or receptors) and sequencing technology errors could introduce unspecific edges into the multi-view CE network. To identify which cell pairs are actively communicating, we proposed a strategy to calculate the edge specificity within each CE network view. Developed from the stLearn permutation test strategy[54], we selected n background gene pairs ($n = 200$ by default) for each ligand–receptor pair. The two genes of each background gene pair have similar average expression levels to the ligand and receptor, respectively. Then we used the background gene pairs to generate the null distribution of each edge and filtered out edges whose weights are not significantly larger than the null distribution (**Supplementary Fig. 1b**).

Specifically, $L'^{(v)}_{a}$ and $R'^{(v)}_{a}$ is the a-th pair of background genes for ligand–receptor pair v, which respectively exhibit close average expression levels with L_v and R_v in the dataset. We calculated the background edge weight between cell i and cell j based on the background gene pair:

$$\omega'^{(v_a)}_{i,j} = e_i^{L'^{(v)}_a} \cdot e_j^{R'^{(v)}_a} \cdot \exp\left[-\left(\frac{dist_{i,j}}{w_{L_v}}\right)^2\right]$$

The edge weights of n background gene pairs $\{\omega'^{(v_1)}_{i,j}, \omega'^{(v_2)}_{i,j}, \ldots, \omega'^{(v_n)}_{i,j}\}$ form the null distribution of $\omega^{(v)}_{i,j}$. We would filter out the edge if $\omega^{(v)}_{i,j}$ isn't larger than enough background edge weights (threshold is set as 0.95 by default). We regarded the proportion of background edge weights that are lower than $\omega^{(v)}_{i,j}$ as the specificity of the edges. In the first breast cancer dataset, removing edges with low specificities reduced the network density in each view of the network, and the mean of connectivity is reduced from 0.173 to 0.046 (**Supplementary Fig. 2b**). Taking COL1A1:DDR1 pair as an example, the detected CE hotspots cover a diffuse region before filtering as both *COL1A1* and *DDR1* are wildly and highly expressed. The hotspots are more clearly defined at the protruding region between parenchyma and stroma after filtering out low-specificity edges (**Supplementary Fig. 2c, d**).

Visualizing CEs based on the multi-view network

CE hotspot

We introduced centrality metrics from social network analysis to visualize the spots with high activities of specific ligand–receptor communication. For the view $G^{(v)}$ in the network G, which represents the CEs via ligand–receptor pair v, we calculated the degree centrality $dc_{i,v}$ and the eigenvector centrality $ec_{i,v}$ for the cell (or spot) i. We used the CE hotspot plot to visualize the centralities of spots.

We obtained the degree centrality $dc_{i,v}$ for cell i and ligand–receptor pair v by summing the indegrees and outdegrees of cell i in $G^{(v)}$:

$$dc_{i,v} = \sum_j \omega^{(v)}_{i,j} + \sum_j \omega^{(v)}_{j,i}$$

where $\omega^{(v)}_{i,j}$ is the edge weight from cell i to cell j in $G^{(v)}$. The indegrees and outdegrees reflect the receiving and sending activities respectively for the corresponding cells. We regarded the in-degree minus out-degree as the sender-receiver attributes, and plotted the attributes in **Fig. 2c**.

As for the eigenvector centrality, we denoted $ec_{i,v}$ as $x_i^{(v)}$ and calculated $ec_{i,v}$ by solving the equation:

$$x_i^{(v)} = c\sum_j (\omega_{i,j}^{(v)} + \omega_{j,i}^{(v)})x_j^{(v)}$$

where c is a constant of proportionality and is set as 1 by default. To obtain a stable $\boldsymbol{x}^{(v)}$, where $\boldsymbol{x}^{(v)} = \left[x_1^{(v)}, x_2^{(v)}, \dots, x_n^{(v)}\right]^T$, each iteration updates $\boldsymbol{x}^{(v)}(t)$ according to:

$$\boldsymbol{x}^{(v)}(t) = c\boldsymbol{A} \times \boldsymbol{x}^{(v)}(t-1)$$

until $\boldsymbol{x}^{(k)}(t) = \boldsymbol{x}^{(k)}(t-1)$.

Cell-type-level CE network

We calculated the cell-type-level CE network to represent the general strengths of CEs from one cell type to another cell type. For ligand–receptor pair v, the edge weight $\omega_{A,B}^{(v)}$ between sender cell type A and receiver cell type B is calculated by summing up the edge weights between cells belonging to cell types A, B in the CE network view $G^{(v)}$:

$$\omega_{A,B}^{(v)} = \sum_{i\in A}\sum_{j\in B}\omega_{i,j}^{(v)}$$

where $\omega_{i,j}^{(v)}$ is the edge weight from cell i to cell j in $G^{(v)}$.

Ligand–receptor pair clustering

Based on the multi-view CE network, we calculated the dissimilarities between pairwise ligand–receptor pairs and identified the ligand–receptor pairs with similar spatial active regions. For two ligand–receptor pairs u and v, we calculated the dissimilarities between them:

$$d_{u,v} = \sqrt{\left(ec_{1,u} - ec_{1,v}\right)^2 + \left(ec_{2,u} - ec_{2,v}\right)^2 + \cdots + \left(ec_{n,u} - ec_{n,v}\right)^2}$$

where $ec_{i,v}$ is the eigenvector centrality for cell i and ligand–receptor pair v, and we used the hierarchical clustering method in sklearn package[55] to cluster ligand–receptor pairs according to the dissimilarities. Then, we summed up the CE hotspots of ligand–receptor pairs in the same cluster, and obtained the cumulated spatial centrality of LR pair clusters. We also performed UMAP dimension reduction for ligand–receptor pairs using the eigenvector centrality matrix and the dissimilarity measurement.

Predicting specific gene expressions via multi-view graph learning

We proposed a graph neural network on the multi-view CE network $\boldsymbol{G}$ to predict the expression profile of specific target genes and interpreted the predicting process to reveal how CEs affect these genes. One of the inputs of the model is the cell-type matrix $\boldsymbol{X} \in R^{N \times C}$, where N is the number of cells, C is the number of cell types and $\boldsymbol{X}$ is the cell-type percentage of each spot or one-hot encoded cell-type labels. Besides, the multi-view CE network G adjacency matrices $\boldsymbol{A} = \left\{\boldsymbol{A}^{(1)}, \boldsymbol{A}^{(2)}, \ldots, \boldsymbol{A}^{(V)}\right\}$ is another input, where $\boldsymbol{A}^{(v)} \in R^{N \times N}$, N is the number of cells and V is the number of views (same as the number of ligand–receptor pairs). The output of the model is the generated gene expression profile $\widehat{\boldsymbol{E}}$. For a target gene t, the model can be described as:

$$\widehat{\boldsymbol{E}} = HoloGNN_t(\boldsymbol{X}, \boldsymbol{A})$$

Selecting target genes to be predicted

We selected genes to be predicted by our model according to the following rules: (1) the genes should be highly variable genes (identified by the *highly_variable_genes* function in Scanpy package[56] using parameters min_mean = 0.05 and min_disp = 0.5); (2) the genes should be expressed in more than 50% cells; (3) the genes should not be mitochondrion genes, ligand or receptor genes. We scaled the expression levels of these genes to 0~1.

Preprocessing adjacency matrices

Cells of the same type that have a close spatial location may have unexpected similarities, for example they may originate from the same progenitor cell. This similarity is dependent on spatial location, but not affected by cell–cell communication, and can interfere with model results as confounding factors. We removed the edges between cells of the same type to remove the confounding factors. We calculated the cell-type similarity ($s_{i,j}$) between cell i, j and the adjusted adjacency matrix ($A'^{(v)}_{ij}$) as:

$$s_{i,j} = \sum_{A} c_i^A c_j^A$$

$$A'^{(v)}_{ij} = (1 - s_{i,j}) A^{(v)}_{ij}$$

where c_i^A represents whether cell i belongs to cell type A, or in spot-based datasets, represents the proportion of cell type A in spot i.

Next, we calculated the normalized adjacency matrix $\hat{A}^{(v)}$ for each network view as:

$$\hat{A}^{(v)} = I + D^{(v)\frac{1}{2}} A'^{(v)} D^{(v)\frac{1}{2}}$$

where $D_{ii}^{(v)} = \sum_j A'^{(v)}_{ij}$.

Graph model architecture

With the cell-type matrix $\boldsymbol{X}$ and preprocessed adjacency matrices $\widehat{\boldsymbol{A}} = \{\hat{A}^{(1)}, \hat{A}^{(2)}, \dots, \hat{A}^{(n)}\}$ as inputs, graph models were constructed to generate the baseline expression $\boldsymbol{E_0}$ determined by its cell type and the expression change $\boldsymbol{\Delta E}$ caused by CEs, and then these two components were summed up to get the expression profile prediction $\widehat{\boldsymbol{E}}$ (**Fig. 1c**).

To estimate $\boldsymbol{\Delta E}$, we used each matrix in $\widehat{\boldsymbol{A}}$ as the adjacency matrix and $\boldsymbol{X}$ as the feature matrix to construct a GNN for each view, and then obtained the embeddings of nodes in each view. Then the embeddings of nodes from each view were integrated with the attention mechanism (learnable weights c_v for each view) to generate the final embeddings $\boldsymbol{Z_\Delta}$:

$$\boldsymbol{Z_\Delta} = ReLU(\sum_v c_v(\hat{A}^{(v)}XW^{(v)} + B^{(v)}))$$

where $\hat{A}^{(v)}X \in R^{N\times C}$ (N is the number of cells and C is the number of cell types) represents the general CE strengths from each sender cell type to each cell via the ligand–receptor pair v, $W^{(v)} \in R^{C\times H}$ (H is the hidden layer dimension and is set as C by default) incorporates the effects from each sender cell type, $B^{(v)} \in R^{N\times H}$ serves as the bias matrix, c_v incorporates effects from each ligand–receptor pair, and *ReLU* is an activation function:

$$ReLU(x) = \begin{cases} x & if\ x \geq 0 \\ 0 & if\ x < 0 \end{cases}$$

Next, we used a fully connected layer to estimate $\boldsymbol{\Delta E}$ ($\boldsymbol{\Delta E} \in R^N$):

$$\widehat{\boldsymbol{\Delta E}} = Linear(\boldsymbol{Z_\Delta})$$

Besides, we constructed another fully connected layer to estimate $\boldsymbol{E_0}$ by the cell-type matrix $\boldsymbol{X}$:

$$\widehat{\boldsymbol{E_0}} = Linear(\boldsymbol{X})$$

And the expression profile prediction $\widehat{\boldsymbol{E}}$ is calculated as:

$$\widehat{\boldsymbol{E}} = Sigmoid(\widehat{\boldsymbol{\Delta E}} + \widehat{\boldsymbol{E_0}})$$

where *Sigmoid* is an activation function:

$$Sigmoid(x) = \frac{1}{1 + e^{-x}}$$

We used the mean squared error (MSE) between $\widehat{\boldsymbol{E}}$ and true expression profile $\boldsymbol{E}$ as the loss function:

$$Loss = MSE(\boldsymbol{E}, \hat{\boldsymbol{E}}) = \frac{1}{n}\sum_{i}(e_i - \hat{e}_i)^2$$

Training strategy

We split cells (or spots) in any dataset into train and validation sets. By default, we used 85% cells as training sets and 15% as validation sets. We trained the model for 500 epochs in the training sets and select the model with the lowest MSE in the validation sets as the final model for the following interpretation. We optimized parameters using the Adam optimizer (initial learning rate is 0.1, and weight decay is 5×10^{-4}) and the StepLR learning rate decay strategy (step size is 10, and gamma is 0.9) by default.

To verify the robustness of the model and improve the reliability of interpretation, we repeatedly trained our graph model for certain times (50 times by default when decoding FCEs and 5 times by default when identifying target genes more affected by cell–cell communication). The final expression profile predictions displayed in the article are the mean value of expression profiles derived from each repetition.

Model interpretation

We obtained a trained model $HoloGNN_t$ for the target gene t after training. We interpreted the model in three ways:

1. **Detecting cell types more affected by FCEs.** We calculated the mean value of $\widehat{\boldsymbol{E_0}}$ and $\widehat{\boldsymbol{\Delta E}}$ from each trained $HoloGNN_t$. And then we calculated $\widehat{\boldsymbol{\Delta E}}/\widehat{\boldsymbol{E_0}}$ for each cell type and regarded cell types with higher $\widehat{\boldsymbol{\Delta E}}/\widehat{\boldsymbol{E_0}}$ as cell types more affected by FCEs.
2. **Identifying ligand–receptor pairs mediating FCEs.** For each trained $HoloGNN_t$, we extracted the view attention c_v which represents the contribution of each view v (corresponding to the ligand–receptor pair v) to the expression profile prediction (**Supplementary Fig. 1c**). We calculated the mean absolute value of c_v in each repeatedly trained $HoloGNN_t$ and plotted these results in the FCE mediator plot.
3. **Identifying the major sender and receiver cell types in FCEs.** As mentioned before, $\hat{A}^{(v)}X$ matrix represents the general CE strengths from each cell type to each cell, and $W^{(v)}$ incorporates the impacts from each sender cell type. Thus, we calculated the general FCE strengths from sender cell type C to the cell i as:

$$\omega_{C,i}^{(v)} = (\hat{A}^{(v)}X)_{i,C} \sum_{k} W_{C,k}^{(v)}$$

The general FCE strengths for each cell type are plotted in **Supplementary Fig. 3**. The computing process is also shown in **Supplementary Fig. 1c**. Also, we summed up the contribution of sender cell type C to all cells of cell type C', and plotted it as the cell-type-level FCE network. The weight of the edge from cell type C to C' in the cell-type-level FCE network is calculated as:

$$\omega_{C,C'}^{(v)} = \sum_{i \in C'} \omega_{C,i}^{(v)}$$

Predicting expression profile with each network view

To verify some ligand–receptor pairs indeed facilitate cells exhibit specific gene expression patterns and remove the multicollinear effect, we predicted the target gene expression profiles with each single view of the CE network. Similar to the $HoloGNN_t$, the architecture of the model using the network view v is:

$$\widehat{\boldsymbol{E}}^{(v)} = Sigmoid\left(Linear\left(ReLU(\hat{A}^{(v)}XW^{(v)} + B^{(v)})\right)\right) + Sigmoid\left(Linear(\boldsymbol{X})\right)$$

$$Loss = MSE(\boldsymbol{E}, \widehat{\boldsymbol{E}}^{(v)})$$

Baseline model

In this article, we used three baseline models: a model only using cell-type information (**Fig. 4**), a model using the spatial proximity relationship matrix rather than a multi-view CE network as the adjacency matrix (**Fig. 3f, Supplementary Fig. 6b**), and a Lasso model with both ligand–receptor communication and cell-type information (**Supplementary Fig. 6c**).

As the first baseline model, we trained a full-connected network using cell type matrix $\boldsymbol{X}$ only, and obtain $\widehat{\boldsymbol{E}}_{only-cell-type}$ according to:

$$\widehat{\boldsymbol{E}}_{only-cell-type} = Sigmoid\left(Linear(X)\right)$$

As the second baseline model, we trained a graph model similar to $HoloGNN_t$ but used the spatial proximity relationship matrix as the adjacency matrix:

$$A_{i,j}^{proximity} = \exp\left[-\left(\frac{dist_{i,j}}{Mean(w_{L_v})}\right)^2\right]$$

We got the preprocessed adjacency matrix $\hat{A}^{proximity}$ in the way discussed before. Then we constructed a graph model and obtained $\widehat{\boldsymbol{E}}_{proximity}$ according to as:

$$\widehat{\boldsymbol{E}}_{proximity} = Sigmoid\left(Linear\left(ReLU(\hat{A}^{proximity}XW + B)\right)\right) + Sigmoid\left(Linear(\boldsymbol{X})\right)$$

The loss function, training strategy and hyperparameters are same as the HoloNet GNN model.

As the third baseline model, we predicted the target gene expression with Lasso regression (‘sklearn’ LassoCV function with default parameters) using both the ligand–receptor communication and cell-type information:

$$\boldsymbol{X}_{v,j}^{(lr)} = \sum_{j} A_{i,j}^{(v)}$$

$$\widehat{\boldsymbol{E}}_{lr} = Lasso([\boldsymbol{X}^{(lr)} || \boldsymbol{X}])$$

where $\boldsymbol{X}$ is the cell-type information, and $||$ represents the concatenation of matrices. We calculated the Pearson correlation of $\widehat{\boldsymbol{E}}_{only-cell-type}$, $\widehat{\boldsymbol{E}}_{proximity}$ and $\widehat{\boldsymbol{E}}_{lr}$ with $\boldsymbol{E}$ as the accuracies of baseline models and compared them with the accuracy of HoloNet GNN model.

Gene ontology enrichment analysis for genes linked to CEs

We characterized the genes more affected or less by cell–cell communication using the ‘clusterProfiler’ R package (version 3.14.3)[57]. We ranked the target genes with the performance improvements after considering CEs. We enriched the top or bottom genes into ‘biological processes’ GO terms, regarding all target genes used to be predicted as the background gene set. The results of enrichment analysis are visualized with the dot plot.

TCGA data analysis

We applied GEPIA[58] to study the gene expression data from the TCGA database. We performed the Pearson’s method to calculate correlation coefficients between expression levels of different genes in TCGA breast cancer data.

Data availability

The used datasets can be downloaded from the 10x Genomics website (https://www.10xgenomics.com/resources/datasets) and Zenodo data repository (https://zenodo.org/record/4739739). The preprocessed public spatial data is available at https://zenodo.org/record/6602473.

Code availability

HoloNet is implemented as a Python package. The code and tutorial of HoloNet are available at https://github.com/lhc17/HoloNet.

References

1. Bonnans, C., Chou, J. & Werb, Z. Remodelling the extracellular matrix in development and disease. *Nat. Rev. Mol. Cell Biol.* (2014). doi:10.1038/nrm3904
2. Armingol, E., Officer, A., Harismendy, O. & Lewis, N. E. Deciphering cell–cell interactions and communication from gene expression. *Nat. Rev. Genet.* (2020). doi:10.1038/s41576-020-00292-x
3. Bich, L., Pradeu, T. & Moreau, J. F. Understanding Multicellularity: The Functional Organization of the Intercellular Space. *Front. Physiol.* (2019). doi:10.3389/fphys.2019.01170
4. Zepp, J. A. *et al.* Distinct Mesenchymal Lineages and Niches Promote Epithelial Self-Renewal and Myofibrogenesis in the Lung. *Cell* (2017). doi:10.1016/j.cell.2017.07.034
5. Niethamer, T. K. *et al.* Defining the role of pulmonary endothelial cell heterogeneity in the response to acute lung injury. *Elife* (2020). doi:10.7554/eLife.53072
6. Harney, A. S. *et al.* Real-time imaging reveals local, transient vascular permeability, and tumor cell intravasation stimulated by TIE2hi macrophage–derived VEGFA. *Cancer Discov.* (2015). doi:10.1158/2159-8290.CD-15-0012
7. Selvey, S. *et al.* Stimulation of MMP-11 (stromelysin-3) expression in mouse fibroblasts by cytokines, collagen and co-culture with human breast cancer cell lines. *BMC Cancer* (2004). doi:10.1186/1471-2407-4-40
8. Roy, S. *et al.* Macrophage-derived neuropilin-2 exhibits novel tumor-promoting functions. *Cancer Res.* (2018). doi:10.1158/0008-5472.CAN-18-0562
9. Liu, C. *et al.* Macrophage-derived CCL5 facilitates immune escape of colorectal cancer cells via the p65/STAT3-CSN5-PD-L1 pathway. *Cell Death Differ.* (2020). doi:10.1038/s41418-019-0460-0
10. Salmén, F. *et al.* Barcoded solid-phase RNA capture for Spatial Transcriptomics profiling in mammalian tissue sections. *Nat. Protoc.* (2018). doi:10.1038/s41596-018-0045-2
11. Ståhl, P. L. *et al.* Visualization and analysis of gene expression in tissue sections by spatial transcriptomics. *Science* (2016). doi:10.1126/science.aaf2403
12. Eng, C. H. L. *et al.* Transcriptome-scale super-resolved imaging in tissues by RNA seqFISH+. *Nature* (2019). doi:10.1038/s41586-019-1049-y
13. Browaeys, R., Saelens, W. & Saeys, Y. NicheNet: modeling intercellular communication by linking ligands to target genes. *Nat. Methods* (2020). doi:10.1038/s41592-019-0667-5
14. Li, D., Ding, J. & Bar-Joseph, Z. Identifying signaling genes in spatial single cell expression data.

Bioinformatics (2020). doi:10.1093/bioinformatics/btaa769

15. Fischer, D. S., Schaar, A. C. & Theis, F. J. Learning cell communication from spatial graphs of cells. *bioRxiv* (2021). doi:10.1101/2021.07.11.451750
16. Wu, S. Z. *et al.* A single-cell and spatially resolved atlas of human breast cancers. *Nat. Genet.* (2021). doi:10.1038/s41588-021-00911-1
17. Stuart, T. *et al.* Comprehensive Integration of Single-Cell Data. *Cell* (2019). doi:10.1016/j.cell.2019.05.031
18. Hou, R., Denisenko, E., Ong, H. T., Ramilowski, J. A. & Forrest, A. R. R. Predicting cell-to-cell communication networks using NATMI. *Nat. Commun.* (2020). doi:10.1038/s41467-020-18873-z
19. Khan, M. R. & Blumenstock, J. E. Multi-GCN: Graph convolutional networks for multi-view networks, with applications to global poverty. in *33rd AAAI Conference on Artificial Intelligence, AAAI 2019, 31st Innovative Applications of Artificial Intelligence Conference, IAAI 2019 and the 9th AAAI Symposium on Educational Advances in Artificial Intelligence, EAAI 2019* (2019). doi:10.1609/aaai.v33i01.3301606
20. Fu, H., Huang, F., Liu, X., Qiu, Y. & Zhang, W. MVGCN: data integration through multi-view graph convolutional network for predicting links in biomedical bipartite networks. *Bioinformatics* (2022). doi:10.1093/bioinformatics/btab651
21. Karaayvaz, M. *et al.* Unravelling subclonal heterogeneity and aggressive disease states in TNBC through single-cell RNA-seq. *Nat. Commun.* (2018). doi:10.1038/s41467-018-06052-0
22. Lehmann, B. D. *et al.* Refinement of triple-negative breast cancer molecular subtypes: Implications for neoadjuvant chemotherapy selection. *PLoS One* (2016). doi:10.1371/journal.pone.0157368
23. Slack, B. E., Siniaia, M. S. & Blusztajn, J. K. Collagen type I selectively activates ectodomain shedding of the discoidin domain receptor 1: Involvement of Src tyrosine kinase. *J. Cell. Biochem.* (2006). doi:10.1002/jcb.20812
24. Das, S. *et al.* Discoidin domain receptor 1 receptor tyrosine kinase induces cyclooxygenase-2 and promotes chemoresistance through nuclear factor-κB pathway activation. *Cancer Res.* (2006). doi:10.1158/0008-5472.CAN-06-1215
25. Sun, X. *et al.* Tumour DDR1 promotes collagen fibre alignment to instigate immune exclusion. *Nature* (2021). doi:10.1038/s41586-021-04057-2
26. Bródka, P., Chmiel, A., Magnani, M. & Ragozini, G. Quantifying layer similarity in multiplex networks: A systematic study. *R. Soc. Open Sci.* (2018). doi:10.1098/rsos.171747
27. Liberzon, A. *et al.* The Molecular Signatures Database Hallmark Gene Set Collection. *Cell Syst.* (2015). doi:10.1016/j.cels.2015.12.004

28. Hood, J. D. & Cheresh, D. A. Role of integrins in cell invasion and migration. *Nat. Rev. Cancer* (2002). doi:10.1038/nrc727

29. Lim, B., Woodward, W. A., Wang, X., Reuben, J. M. & Ueno, N. T. Inflammatory breast cancer biology: the tumour microenvironment is key. *Nat. Rev. Cancer* (2018). doi:10.1038/s41568-018-0010-y

30. Basset, P. *et al.* A novel metalloproteinase gene specifically expressed in stromal cells of breast carcinomas. *Nature* (1990). doi:10.1038/348699a0

31. Zhang, X. *et al.* Insights into the distinct roles of MMP-11 in tumor biology and future therapeutics (Review). *Int. J. Oncol.* (2016). doi:10.3892/ijo.2016.3400

32. Min, K. W. *et al.* Diagnostic and prognostic relevance of mmp-11 expression in the stromal fibroblast-like cells adjacent to invasive ductal carcinoma of the breast. *Ann. Surg. Oncol.* (2013). doi:10.1245/s10434-012-2734-3

33. González-González, L. & Alonso, J. Periostin: A matricellular protein with multiple functions in cancer development and progression. *Front. Oncol.* (2018). doi:10.3389/fonc.2018.00225

34. Shao, R. *et al.* Acquired Expression of Periostin by Human Breast Cancers Promotes Tumor Angiogenesis through Up-Regulation of Vascular Endothelial Growth Factor Receptor 2 Expression. *Mol. Cell. Biol.* (2004). doi:10.1128/mcb.24.9.3992-4003.2004

35. Lambert, A. W. *et al.* Tumor cell-derived periostin regulates cytokines that maintain breast cancer stem cells. *Mol. Cancer Res.* (2016). doi:10.1158/1541-7786.MCR-15-0079

36. Kim, G. E., Lee, J. S., Park, M. H. & Yoon, J. H. Epithelial periostin expression is correlated with poor survival in patients with invasive breast carcinoma. *PLoS One* (2017). doi:10.1371/journal.pone.0187635

37. Cui, N. P. *et al.* Protein Tyrosine Kinase 7 Regulates EGFR/Akt Signaling Pathway and Correlates With Malignant Progression in Triple-Negative Breast Cancer. *Front. Oncol.* (2021). doi:10.3389/fonc.2021.699889

38. Yu, B. *et al.* Periostin secreted by cancer-associated fibroblasts promotes cancer stemness in head and neck cancer by activating protein tyrosine kinase 7. *Cell Death Dis.* (2018). doi:10.1038/s41419-018-1116-6

39. Damelin, M. *et al.* A PTK7-targeted antibody-drug conjugate reduces tumor-initiating cells and induces sustained tumor regressions. *Sci. Transl. Med.* (2017). doi:10.1126/scitranslmed.aag2611

40. Pal, S. K. *et al.* THBS1 is induced by TGFB1 in the cancer stroma and promotes invasion of oral squamous cell carcinoma. *J. Oral Pathol. Med.* (2016). doi:10.1111/jop.12430

41. Schuetz, C. S. *et al.* Progression-specific genes identified by expression profiling of matched ductal carcinomas in situ and invasive breast tumors, combining laser capture microdissection and

oligonucleotide microarray analysis. *Cancer Res.* (2006). doi:10.1158/0008-5472.CAN-05-4610

42. Kim, H., Watkinson, J., Varadan, V. & Anastassiou, D. Multi-cancer computational analysis reveals invasion-associated variant of desmoplastic reaction involving INHBA, THBS2 and COL11A1. *BMC Med. Genomics* (2010). doi:10.1186/1755-8794-3-51

43. Jin, L., Shen, F., Weinfeld, M. & Sergi, C. Insulin Growth Factor Binding Protein 7 (IGFBP7)-Related Cancer and IGFBP3 and IGFBP7 Crosstalk. *Front. Oncol.* (2020). doi:10.3389/fonc.2020.00727

44. Benatar, T. *et al.* IGFBP7 reduces breast tumor growth by induction of senescence and apoptosis pathways. *Breast Cancer Res. Treat.* (2012). doi:10.1007/s10549-011-1816-4

45. Zuo, S. *et al.* IGFBP-rP1 induces p21 expression through a p53-independent pathway, leading to cellular senescence of MCF-7 breast cancer cells. *J. Cancer Res. Clin. Oncol.* (2012). doi:10.1007/s00432-012-1153-y

46. Hooper, A. T. *et al.* Angiomodulin Is a Specific Marker of Vasculature and Regulates Vascular Endothelial Growth Factor-A-Dependent Neoangiogenesis. *Circ. Res.* (2009). doi:10.1161/CIRCRESAHA.109.196790

47. Nicosia, R. F., Belser, P., Bonanno, E. & Diven, J. Regulation of angiogenesis in vitro by collagen metabolism. *Vitr. Cell. Dev. Biol. - Anim.* (1991). doi:10.1007/BF02631124

48. Bonanno, E., Jurlaro, M., Madri, J. A. & Nicosia, R. F. Type IV collagen modulates angiogenesis and neovessel survival in the rat aorta model. *Vitr. Cell. Dev. Biol. - Anim.* (2000). doi:10.1290/1071-2690(2000)036<0336:ticmaa>2.0.co;2

49. Chen, K. H., Boettiger, A. N., Moffitt, J. R., Wang, S. & Zhuang, X. Spatially resolved, highly multiplexed RNA profiling in single cells. *Science* (2015). doi:10.1126/science.aaa6090

50. Shi, Y. *et al.* Dynamics of large multi-view social networks: Synergy, cannibalization and cross-view interplay. in *Proceedings of the ACM SIGKDD International Conference on Knowledge Discovery and Data Mining* (2016). doi:10.1145/2939672.2939814

51. Kivelä, M. *et al.* Multilayer networks. *J. Complex Networks* (2014). doi:10.1093/comnet/cnu016

52. Paszke, A. *et al.* PyTorch: An imperative style, high-performance deep learning library. in *Advances in Neural Information Processing Systems* (2019).

53. Balluffi, R. W., Allen, S. M. & Carter, W. C. *Kinetics of Materials*. *Kinetics of Materials* (2005). doi:10.1002/0471749311

54. Pham, D. *et al.* stLearn: integrating spatial location, tissue morphology and gene expression to find cell types, cell-cell interactions and spatial trajectories within undissociated tissues. *bioRxiv* (2020). doi:10.1101/2020.05.31.125658

55. Pedregosa, F. *et al.* Scikit-learn: Machine learning in Python. *J. Mach. Learn. Res.* (2011).

56. Wolf, F. A., Angerer, P. & Theis, F. J. SCANPY: Large-scale single-cell gene expression data analysis. *Genome Biol.* (2018). doi:10.1186/s13059-017-1382-0

57. Yu, G., Wang, L. G., Han, Y. & He, Q. Y. ClusterProfiler: An R package for comparing biological themes among gene clusters. *Omi. A J. Integr. Biol.* (2012). doi:10.1089/omi.2011.0118

58. Tang, Z. *et al.* GEPIA: A web server for cancer and normal gene expression profiling and interactive analyses. *Nucleic Acids Res.* (2017). doi:10.1093/nar/gkx247

Acknowledgments

We thank Sijie Chen, Haoxiang Gao, Jiaqi Li, Chen Li, Xi Xi, Haiyang Bian, and Yixin Chen for helpful discussions.

The work is supported in part by National Key R&D Program of China grant 2021YFF1200900, NSFC grants 62050178, 61721003, 32000453, 42050101 and 62103227.

Author contributions

H.L., M.H., T.M., L.W., X.Z. conceived the study. L.W. and X.Z. supervised the research. H.L. designed and implemented the algorithm. H.L. and T.M. prepared the figures. H.L., L.W., and X.Z. wrote the manuscript.

Competing interests

The authors declare no competing interests.